Structure-activity relationships in metal organic framework derived mesoporous nitrogen-doped carbon containing atomically dispersed iron sites for CO_2 electrochemical reduction

Sun, Xiaohui; Wang, Riming; Ould-Chikh, Samy; Osadchii, Dmitrii; Li, Guanna; Aguilar, Antonio; Hazemann, Jean louis; Kapteijn, Freek; Gascon, Jorge

Important note
To cite this publication, please use the final published version (if applicable).
Please check the document version above.

Structure-Activity Relationships in Metal Organic Framework Derived Mesoporous Nitrogen-doped Carbon Containing Atomically Dispersed Iron Sites for CO₂ Electrochemical Reduction

Xiaohui Sun[1], Riming Wang[1], Samy Ould-Chikh[2], Dmitrii Osadchii[1], Guanna Li[1], Antonio Aguilar[3], Jean-louis Hazemann[3], Freek Kapteijn[1], and Jorge Gascon[1,2] **

[1]*Catalysis Engineering, Department of Chemical Engineering, Delft University of Technology, Van der Maasweg 9, 2629 HZ Delft, The Netherlands*

[2] *Advanced Catalytic Materials, KAUST Catalysis Center, King Abdullah University of Science and Technology, Thuwal 23955, Saudi Arabia*

[3] *Inst. Néel, UPR 2940 CNRS - Univ. Grenoble Alpes, F-38000 Grenoble, France*

* Correspondence to: F.Kapteijn@tudelft.nl; jorge.gascon@kaust.edu.sa;

Abstract: Mesoporous nitrogen-doped carbon nanoparticles with atomically dispersed iron sites (named mesoNC-Fe) are synthesized *via* high-temperature pyrolysis of an Fe containing ZIF-8 MOF. Hydrolysis of tetramethyl orthosilicate (TMOS) in the MOF framework prior to pyrolysis plays an essential role in maintaining a high surface area during the formation of the carbon structure, impeding the formation of iron (oxide) nanoparticles. To gain inside on the nature of the resulting atomically dispersed Fe moieties, HERFD-XANES, EXAFS and valence-to-core X-ray emission spectroscopies have been used. The experimental spectra (both XAS and XES) combined with theoretical calculations suggest that iron has a coordination sphere including a porphyrinic environment and OH/H₂O moieties responsible for the high activity in CO₂ electroreduction. DFT calculations demonstrate that CO formation is favored in these structures because the free energy barriers of *COOH formation are decreased and the adsorption of *H is impeded. The combination of such a unique coordination environment with a high surface area in the carbon structure of mesoNC-Fe makes more active sites accessible during catalysis and promotes CO₂ electroreduction.

Keywords: CO₂, CO, electroreduction, atomically dispersed sites, iron.

1. INTRODUCTION

The increasing global demand for energy has inevitably led to rising CO_2 emissions due to the combustion of fossil fuels (*e.g.* coal, petroleum and natural gas), which is considered to accelerate global warming and climate deterioration.[1] Two major approaches can be followed to decrease CO_2 content in the atmosphere: to capture and geologically sequestrate CO_2, or to convert CO_2 into valuable chemical fuels. Obviously the latter approach seems to be more attractive, especially considering potential leaks of stored CO_2.[2, 3] Various catalytic approaches for CO_2 reduction, such as thermocatalytic reduction, photocatalytic reduction and electrocatalytic reduction have been proposed.[4-6]

Numerous metal catalysts are active in CO_2 electroreduction, such as Au, Ag, Cu *etc*.[7-9] The catalytic performances of different metals were found to depend on the binding energy between the metal atoms and CO, an intermediate in CO_2 reduction. Metals that bind CO strongly can be poisoned by CO or may lead to the formation of other intermediates during CO_2 reduction, resulting in a high product selectivity toward H_2, by the competitive hydrogen evolution reaction (HER) in the aqueous medium.[10] Metals having an intermediate binding energy with CO are found to be active in the synthesis of hydrocarbons and oxygenates that require a transfer of more than two electrons.[9] When the binding energy between the metal and CO becomes weak, CO is the main product, as CO molecules can easily desorb from the metal surface prior to further reduction to alcohols and/or hydrocarbons.[11] In the last case, in order to obtain target fuels and other valuable chemicals, an additional hydrogenation of CO *via* heterogeneous catalysis processes (*e.g.* Fischer-Tropsch synthesis) would be needed.[12, 13]

Nitrogen-doped carbon (hereafter denoted as NC) supported transition metal catalysts exhibit unique chemical and electrical properties, and are supposed to act as alternatives to expensive noble metal catalysts in electrocatalysis.[14, 15] Interestingly, the catalytic activity and product selectivity to a large extent depend on the configuration of the transition metal in the carbon framework. For instance, iron nanoparticles anchored on NC supports were reported to mainly produce H_2.[16] In contrast, atomically dispersed iron atoms prefer to bond with heteroatoms, such as N, C and/or O in the carbon matrix, and CO is the primary product from these isolated iron sites.[14] Until now, extensive efforts have been made to understand the local structure of these atomically dispersed metal sites in the NC matrixes, and the coordination environment of metal centers largely depends on the materials and methods of preparation.[17-19]

As a subclass of metal organic frameworks (MOFs), zeolitic imidazolate frameworks (ZIFs) have recently emerged as promising templates to synthesize novel materials, because of their unique textural properties and atomic metal dispersion.[20, 21] For instance, NC with atomically dispersed metal sites in the framework has been successfully prepared by adding little amount of their inorganic metal salts in the synthesis solution of ZIF-8, followed by thermal treatment at high temperature under inert atmosphere.[22, 23] The preferred formation of these atomically dispersed metal sites can be attributed to the generation of free N-coordination sites in the carbon matrix after Zn evaporates, which helps to stabilize the foreign metal atoms (FMA).[23, 24] However, thermal treatment at high temperature inevitably causes severe fusion and aggregation of carbon nanoparticles, which shows low surface area and pore volume, and therefore reduces the number of accessible active sites during catalysis.[25, 26]

Herein, we report a facile approach to prepare mesoporous NC with atomically dispersed iron sites (mesoNC-Fe). This approach consists of (*i*) hydrolysis of tetramethyl orthosilicate (TMOS) in the structure of an iron-containing ZIF-8 material (ZIF-8-Fe), (*ii*) high-temperature pyrolysis and (*iii*) SiO_2 template leaching. The SiO_2-assisted approach is vital to (*i*) inhibit the formation of iron nanoparticles, (*ii*) preferentially generate atomically dispersed iron sites, and (*iii*) create high surface area and mesoporosity in the carbon matrix. This catalyst was tested in CO_2 electroreduction and showed high CO Faradaic efficiency (FE_{CO}), partial current density of CO (j_{CO}) and good catalytic stability. Because of the non-crystalline nature of the iron active phase, specific X-ray spectroscopies are applied to unravel the chemical environment of iron: HERFD-XANES, EXAFS and valence-to-core X-ray emission spectroscopies. Comparison of the experimental spectra (both XAS and XES) with the theoretical spectra calculated for various plausible models, allowed us to approximate to the coordination sphere of iron.

2. EXPERIMENTAL

2.1. Materials

2-Methylimidazole (MeIm, purity 99%), zinc nitrate hexahydrate ($Zn(NO_3)_2 \cdot 6H_2O$, >98%), iron nitrate nonahydrate ($Fe(NO_3)_3 \cdot 9H_2O$, >99%), tetramethyl orthosilicate (TMOS ≥99%), and methanol (>99.8%) were purchased from Sigma-Aldrich Chemical Co. All the chemicals were used without further purification.

2.2 Catalyst synthesis

For the synthesis of ZIF-8-Fe, a mixture of $Zn(NO_3)_2 \cdot 6H_2O$ and $Fe(NO_3)_3 \cdot 9H_2O$ with Zn/Fe molar ratio of 25 (n_{Zn}/n_{Fe}=25) was dissolved in 200 mL methanol. A mixture of MeIm (6.489 g) in 200 mL methanol was rapidly poured into the above solution with vigorous stirring for 24 h at room temperature. The total molar amount of (Zn + Fe) was fixed to be 10 mmol. Afterwards, the products were collected by filtration, washed thoroughly with methanol, and dried overnight at 80 °C under vacuum.

For the preparation of ZIF-8-Fe@SiO_2, 1 g ZIF-8-Fe was suspended in 5 mL TMOS in an autoclave, and further transferred into a rotation oven and heated up to 333 K and kept at 333 K overnight. After the oven was cooled down to room temperature, the mixture was carefully washed with ethanol by filtration. Then the obtained ZIF-8-Fe@TMOS material was placed in a cotton thimble of 22 mm diameter inside a glass tube of 25 mm diameter. The glass tube was fitted to a round bottom flask containing 500 mL water. A needle to bubble ~10 ml min^{-1} N_2 flow into water was also fitted. The temperature was raised to 50 °C to create a wet N_2 stream to hydrolyze the TMOS molecules for 24 h, after which the sample was collected and dried in an oven at 60 °C overnight.

NC-Fe@SiO_2 was prepared by pyrolysis of 1 g ZIF-8-Fe@SiO_2 at 900 °C for 4 h under N_2 at a ramp of 2 °C min^{-1} in a ceramic crucible inside a quartz tubular reactor (approx. L = 1.0 m × ID = 4.0 cm) horizontally situated in a ceramic fiber oven (Carbolite, Sheffield). The obtained NC-Fe@SiO_2 was further leached in 1 M NaOH solution for 24 h to remove the SiO_2 template, followed by washing with deionized water until the pH reached neutral, and dried at 50 °C overnight under vacuum to yield mesoNC-Fe.

As reference, mesoNC was prepared by hydrolysis of TMOS in ZIF-8, followed by pyrolysis and SiO_2 leaching under the same conditions as the preparation of mesoNC-Fe. Further for comparison, microNC and microNC-Fe were prepared by direct pyrolysis of 1 g ZIF-8 and ZIF-8-Fe, respectively, at 900 °C for 4 h.

2.3. Characterization

Transmission electron microscopy (TEM) and high-resolution TEM (HR-TEM) were performed by using a Talos F200X microscope (FEI, Hillsboro, OR, USA) at an acceleration voltage of 200 kV. X-ray diffraction (XRD) patterns were recorded on a Bruker D8 Advance X-ray diffractometer equipped with a Co-$K\alpha$ radiation (λ = 0.179026 nm). Raman spectra analysis was performed by using a commercial Renishaw in Via Reflex confocal microscope with a 532 nm laser. The N_2 adsorption-desorption isotherms were measured at 77 K using a Micromeritics Tristar 3020 apparatus. Prior to measurement, samples were degassed under

vacuum at 383 K overnight. XPS measurements were performed on a *K*-alpha Thermo Fisher Scientific spectrometer using monochromatic Al-*Kα* radiation at ambient temperature and chamber pressure of about 10^{-8} mbar. All the spectra measured were corrected by setting the reference binding energy of carbon (*1s*) at 284.8 eV. Spectra were analyzed using the Thermo Avantage software package. Background subtraction was done using the setting "SMART" (based on the Shirley background with the additional constraint that the background should not be of a greater intensity than the actual data at any point in the region). The deconvolution of spectra was performed using a mixed Gauss-Lorentz function where the Lorentzian contribution was set to 20%. Linear sweep voltammetry (LSV) was conducted with a potentiostat (Autolab PGSTAT302N) in the potential range of 0.40 V to -1.40 V vs. Ag/AgCl at a sweep rate of 0.05 V s^{-1}.

2.4. Catalyst performance

For the preparation of the electrode, 50 mg catalyst was suspended in a mixture of tetrahydrofuran (4 mL), Nafion solution (0.5 mL), and isopropyl alcohol (4 mL). This mixture was transferred to an ultrasonic bath and kept for 2 h. The suspension was drop-casted onto a carbon cloth electrode with an area (two-sided) of 12.5 cm^2 (2.5 cm × 2.5 cm). The electrode was then dried overnight at 80 °C under evacuation.

CO_2 electrochemical reduction experiments were performed in the previously described continuous flow reactor.[27] A proton-exchange membrane separated reactor into an anode and cathode compartment. The anode compartment contained a counter electrode (Pt gauze), whereas the cathode compartment contained the working electrode and a reference electrode (Ag/AgCl electrode). Both compartments had a volume of 100 mL and were filled with 85 mL of 0.1 M KHCO$_3$ prior to the performance tests, leaving a headspace of 15 mL. CO_2 was then fed into the reactor by bubbling through the liquid with a flow rate of 100 mL min^{-1} until the electrolyte was saturated, after which the CO_2 flow was fixed at 10 mL min^{-1}. An operation potential was applied by a potentiostat (Autolab PGSTAT302N) in the range of -1.0 to -2.0 V versus Ag/AgCl to initiate the controlled potential electrolysis. The cathode compartment was connected to an online gas chromatograph (GC, Global Analyzer Solution Compact GC) to analyze the gas product. All experiments lasted 120 min, and for each potential applied in the controlled potential performance test, a new electrode was prepared. At the end of the electrocatalytic test, a liquid sample (~1 mL) was collected from the electrolyte solution for ultraperformance liquid chromatography (UPLC) measurements. After each experiment, the electrochemical reactor was cleaned with distilled water and the proton-exchange membrane was immersed into 0.1 M H$_2$SO$_4$ for regeneration.

The Faradaic efficiency (*FE*) of the gas product was calculated on the basis of the following equation:

$$FE = \frac{(n \times F \times v \times f)}{j} \tag{1}$$

where n is the number of electrons consumed to produce one product molecule, for the product of CO or H_2, $n = 2$; v is the molar fraction of a certain gas product; f is the overall gas molar flow rate (mol s^{-1}); F is the Faraday constant ($F = 96\ 485$ C mol^{-1}); j is the steady-state cell current at each applied potential (A).

3. RESULTS AND DISCUSSION

3.1. Characterization of the as-synthesized mesoNC-Fe catalyst

Fig. 1 illustrates the preparation process for mesoNC-Fe. In the first step, ZIF-8-Fe was synthesized by adding Fe(NO$_3$)$_3$ into a solution containing Zn(NO$_3$)$_2$, 2-methylimidazole (MeIm) and methanol. Then tetramethyl orthosilicate (TMOS) was hydrolyzed in the structure of ZIF-8-Fe, followed by pyrolysis under N$_2$ and SiO$_2$ leaching with a NaOH solution to generate the mesoNC-Fe catalyst (see Experimental Section for the details).
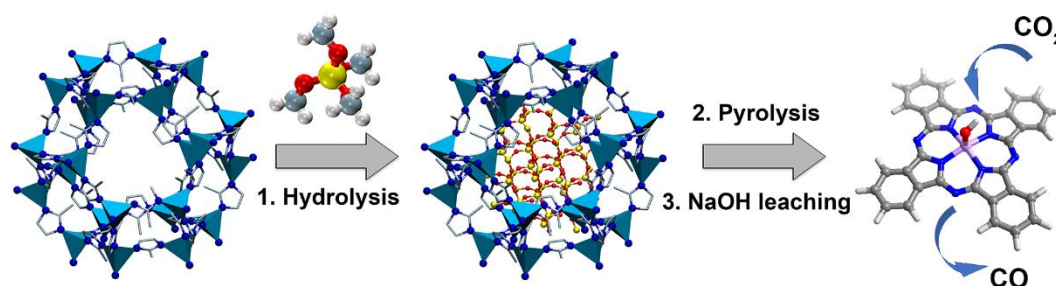
Fig. 1. Schematic illustration of the synthesis of the mesoNC-Fe catalyst. (1) Impregnation and hydrolysis of TMOS molecules in ZIF-8-Fe. (2) Pyrolysis of ZIF-8-Fe@SiO$_2$ in N$_2$ to decompose ZIF-8-Fe and form NC-Fe@SiO$_2$. (3) NaOH leaching to remove SiO$_2$ to generate the mesoNC-Fe catalyst.

The structure of the synthesized ZIF-8-Fe was analyzed by XRD, which matches well with that of ZIF-8 (Fig. S2). Hydrolysis of TMOS led to a homogeneous dispersion of Si in the structure of ZIF-8-Fe (Fig. S3). After a following pyrolysis and a subsequent NaOH leaching, mesoNC-Fe is obtained. Metal (oxide) nanoparticles can hardly be observed in mesoNC-Fe, suggesting a high dispersion state of metal in the carbon matrix (Fig. 2a, b). X-ray spectroscopy (EDX) further validates a uniform dispersion of C, N and Fe throughout the carbon matrix (Fig. 2c-e). In contrast, iron (oxide) nanoparticles are present in microNC-Fe (Fig. S4a), highlighting the important role of SiO$_2$ to inhibit the agglomeration of iron atoms

to form nanoparticles during high temperature pyrolysis. The absence of iron (oxide) nanoparticles in mesoNC-Fe is further supported by powder XRD analysis, where only two broad reflections at $2\Theta = 30\,°$ and $50.5\,°$ are identified, ascribed to the (002) and (100) planes of carbon, respectively (Fig. 3a).[28] Raman spectra of all these as-synthesized materials (Fig. S4d) exhibit two peaks at around $1350\,cm^{-1}$ and $1580\,cm^{-1}$, which can be correlated to graphitic disordered or defective carbon (D-band) and sp^2-bonded graphitic carbon sheets (G-band), respectively.[21] These samples exhibit similar intensity ratio between D band and G band (I_D/I_G), suggesting a similar degree of (dis-)order.
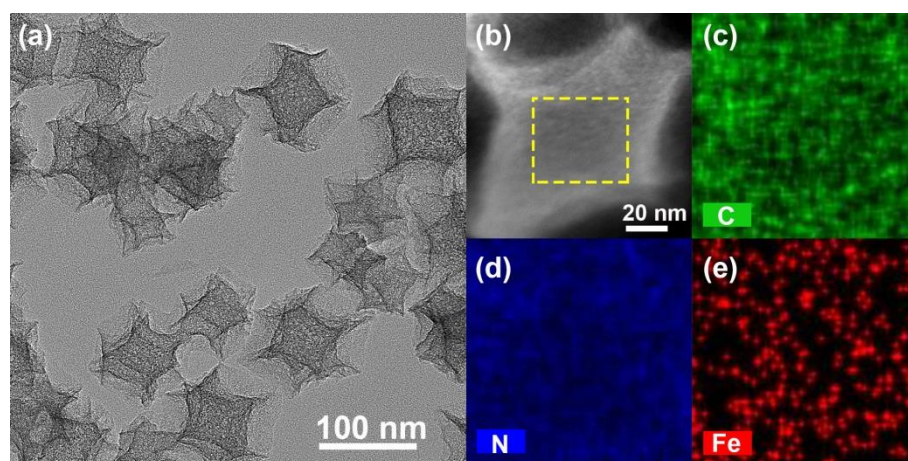
Fig. 2: Bright field TEM and dark field STEM images of mesoNC-Fe (a, b); EDX mapping of C, N and Fe (c-e).

The parent ZIF-8 and ZIF-8-Fe samples have a high BET area (S_{BET}) and pore volume (V_{pore}), and display a typical microporous structure with intergranular mesoporosity, as indicated by the steep N_2 uptake at low relative pressures and the hysteresis loop above $P/P_0 \approx$ 0.8, respectively (Fig. S5a).[29] The mesoNC and mesoNC-Fe samples exhibit a slightly lower S_{BET} and V_{pore} than their parent ZIFs, probably attributed to the collapse of the well-defined microporous structure of ZIF materials and slight agglomeration of nanoparticles during pyrolysis (Fig. 3b and Fig. S5b). At the same time, an H_3 hysteresis loop that closes at $P/P_0 \approx 0.4$ can be as well observed, suggesting the presence of ill-defined mesopores in mesoNC and mesoNC-Fe. In contrast, microNC and microNC-Fe show a much lower S_{BET} and V_{pore} (Table S1), ascribed to the more severe destruction of the ZIF nanoparticles during pyrolysis in the absence of SiO_2. The XPS survey data prove the presence of C, N, O, Fe (depending on the sample) and Zn in these samples without detectable Si and Na (Table S2). The residual Zn signals in the pyrolyzed samples have been demonstrated to be porphyrin-like Zn ($Zn-N_x$) species in the nitrogen doped carbon matrix.[30] The N$1s$ spectra were

deconvoluted into four types of species with binding energies around 398.5 eV, 399.9 eV, 400.9 eV, and 402.4 eV, attributed to pyridinic-N, pyrrolic-N, quaternary-N and oxidized-N, respectively (Fig. 3c and Fig. S6a-c).[31] Obviously, pyridinic-N dominates in all these samples.
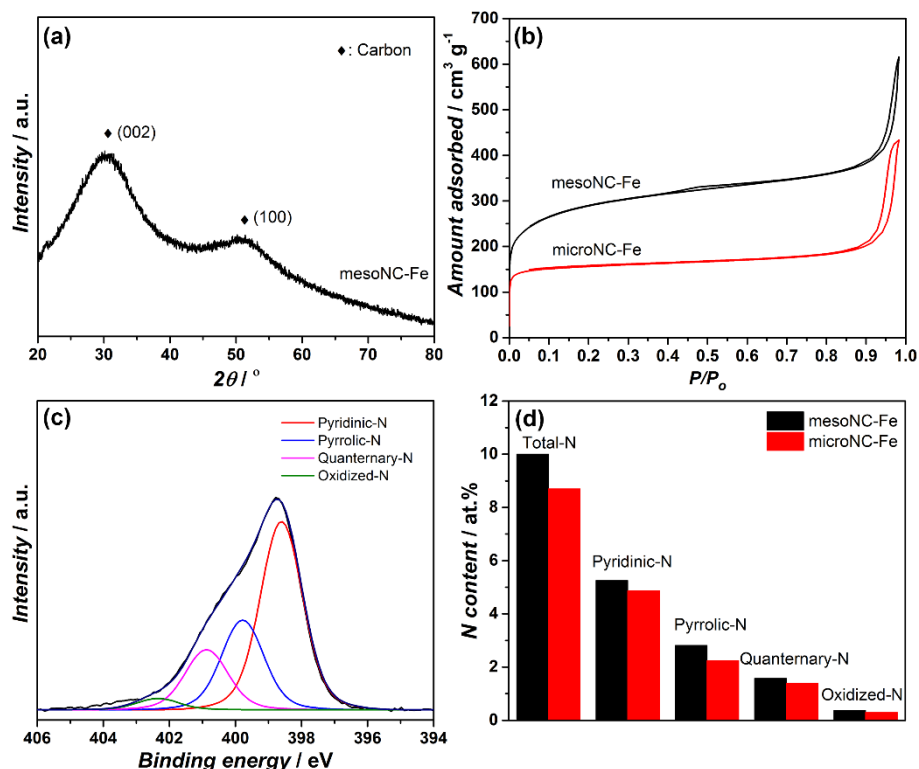
Fig. 3: X-ray diffraction (XRD) patterns of mesoNC-Fe (a); N_2-sorption isotherms of mesoNC-Fe and microNC-Fe (b); N$1s$ XPS regions of mesoNC-Fe with deconvolution into the N-speciation (c) and N distribution mesoNC-Fe and microNC-Fe (d).

3.2. Exploring the coordination environment of iron sites in mesoNC-Fe

X-ray absorption spectroscopy (XAS) was further performed at Fe K-edge to explore the structural and valence information of iron in mesoNC-Fe. As shown in Fig. 4a, simple qualitative comparison of the XANES data with selected references indicates that the spectrum of mesoNC-Fe is almost identical to that of $[Fe(H_2O)_6]^{3+}$ in solution.[32] A common statement of the structure of iron doped in nitrogen-doped carbon is Fe-N$_4$ pyridinic moieties in a square planar configuration.[33] In that case, a sharp pre-edge peak around 7,118 eV is present (*cf.* the XANES spectrum of FePc, Fig. 4a), due to the Fe($1s$) → Fe($4p_z$) transition coupled to a ligand-to-metal charge transfer (shake-down).[34] However, the latter pre-edge feature is absent from the spectrum of mesoNC-Fe, indicative of at least a broken D$_{4h}$ symmetry or an O$_h$ symmetry. Instead, a weak and broad peak is observed at 7115 eV in the pre-edge region due to Fe($1s$) → Fe($3d$) transitions as in the $[Fe(H_2O)_6]^{3+}$ spectrum. These

transitions gain their intensity *via* quadrupolar coupling or by *3d-4p* mixing in distorted octahedral field. The position of the pre-edge is also consistent with a trivalent iron.[35, 36]

The FT-EXAFS spectrum of mesoNC-Fe displays a main peak that is typical of metal-ligand distance ($\approx$ 1.5 Å, no phase correction, Fig. 4b). Comparison with the EXAFS spectra of standards also points towards structural similarities with $[Fe(H_2O)_6]^{3+}$ in solution. However, there is an additional weak peak at 2.8 Å which may arise from a Fe-Fe scattering path as suggested by the comparison with the iron oxide references. Consequently, several models based on the combination of various scattering paths (Fe-O, Fe-N, Fe-C, Fe-Si, Fe-Fe, Fe-Zn) were tested to perform the quantitative analysis of the EXAFS data. The best-fit model includes a Fe-N scattering path for the first shell and a Fe-C scattering path for the second shell (Table S4). Note that the Fe-N scattering path also accounts for the presence of oxygen atoms since nitrogen and oxygen are indistinguishable by EXAFS spectroscopy.[37] The final parameters extracted from the EXAFS fit indicate a Fe-O/N bond at 1.96 $\pm$ 0.03 Å with a coordination number (*CN*) of 5.6 $\pm$ 1.2, and a Fe-C bond at 2.98 $\pm$ 0.04 Å (*CN* = 7.2 $\pm$ 2.4). Importantly, in the fittings of the EXAFS signal for mesoNC-Fe, it was not possible to include Fe-Fe scattering paths with reasonable parameters. Therefore, the negligible contribution of Fe-Fe scattering paths further confirms that nanocrystals are barely present in mesoNC-Fe.
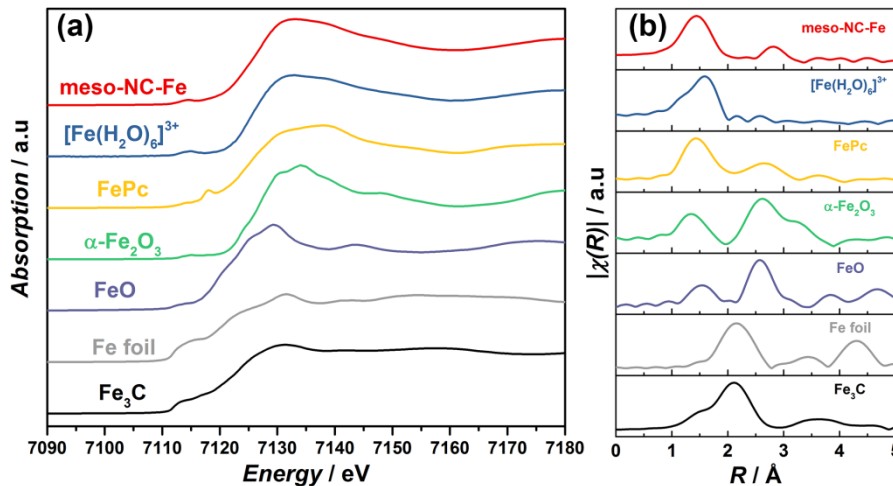
Fig. 4: (a) Fe K-edge XANES spectra and (b) FT-EXAFS $k^2.\chi(k)$ functions for meso-NC-Fe, $[Fe(H_2O)_6]^{3+}$ in water (0.01M), FePc, α-Fe$_2$O$_3$, FeO, Fe foil, and Fe$_3$C. Spectrum of $[Fe(H_2O)_6]^{3+}$ in water was retrieved from the <u>F. W. Lytle database</u>: the International X-ray absorption society website at http://ixs.iit.edu/database/; and the spectrum of FePc was kindly provided by Zitolo, *et al.*[19]

Thus, XANES and EXAFS spectroscopies rule out the reduction of iron to its carbidic or metallic state, exclude the square-planar configuration of a simple Fe-N$_4$ moiety, and confirm a high dispersion of atomic iron in its trivalent state in mesoNC-Fe. Note that during the

investigation of various EXAFS models, it was possible to obtain reasonable agreement using five- or six-coordinated iron (square pyramidal or octahedral geometry). Furthermore, previous characterizations on similar materials proposed various alternative structures: the coordination of the Fe-N$_4$ moiety is often expanded by a water molecule, hydroxyl group or molecular dioxygen (for ORR studies).[19, 38, 39] Given the on-going debate on the structure of iron active sites immobilized on nitrogen-doped graphene and the limits of the above characterization, valence-to-core X-ray emission spectroscopy and HERFD-XANES spectroscopy coupled to DFT calculations were conducted to further refine our structural model.[40]
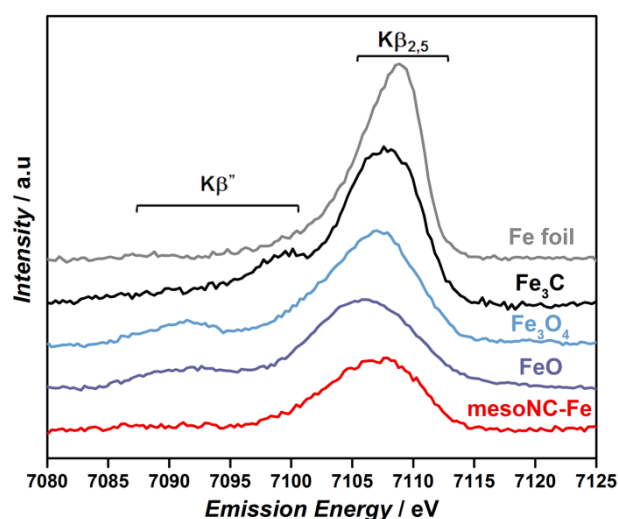
Fig. 5: VTC-$K\beta$ spectra for a selected set of Fe-based compounds and mesoNC-Fe after removal of the $K\beta_{1,3}$ background.

Non-resonant X-ray emission spectroscopy starts with the ionization of $1s$ electron on iron by incident X-ray photons with energies well-above the K-edge energy threshold. Then, an electron decays to fill the $1s$ core-hole with a simultaneous emission of photons.[41] The VTC-XES spectrum arises from transitions from occupied orbitals a few eV below the Fermi level (the valence band for solids or the highest occupied molecular orbitals for complexes). This valence-to-core region is traditionally divided into two emission lines: the Kβ" and K$\beta_{2,5}$ transitions which are respectively attributed to orbitals mixed metal-ligand ns and np states. One of the first application of VTC-XES for chemistry is related to the sensitivity in energy position of the $K\beta$" peak which depends of the identity of the ligand (*e.g.* C, N, O, S).[42-45] Since the XANES spectrum of mesoNC-Fe is similar to the spectrum of [Fe(H$_2$O)$_6$]$^{3+}$ cation, we had suspicions that nitrogen atoms are not even coordinated to iron despite the XPS spectroscopic evidence of a significant amount of pyridinic nitrogen. Thus, the initial

motivation for the XES study was to overcome the limitation of EXAFS concerning the discrimination between oxygen and nitrogen atoms. The VTC-$K\beta$ spectrum of mesoNC-Fe is shown in Fig. 5 with several standards for comparison (Fe foil, Fe_3C, Fe_3O_4, FeO). Unexpectedly, the VTC-$K\beta$ spectrum of mesoNC-Fe presents only a broad peak centered at $\approx$ 7107 eV in the $K\beta_{2,5}$ region with no clear peak in the $K\beta$'' region (within the accuracy limits of the background removal). On the other hand, the iron oxides (FeO and Fe_3O_4) and iron carbide (Fe_3C) spectra clearly highlight a $K\beta$'' contribution respectively centered at 7091 and 7099 eV. For the iron foil (α-Fe, bcc structure), there is no observable $K\beta$'' contribution, confirming that $K\beta$'' mainly comes from the ligand s states.
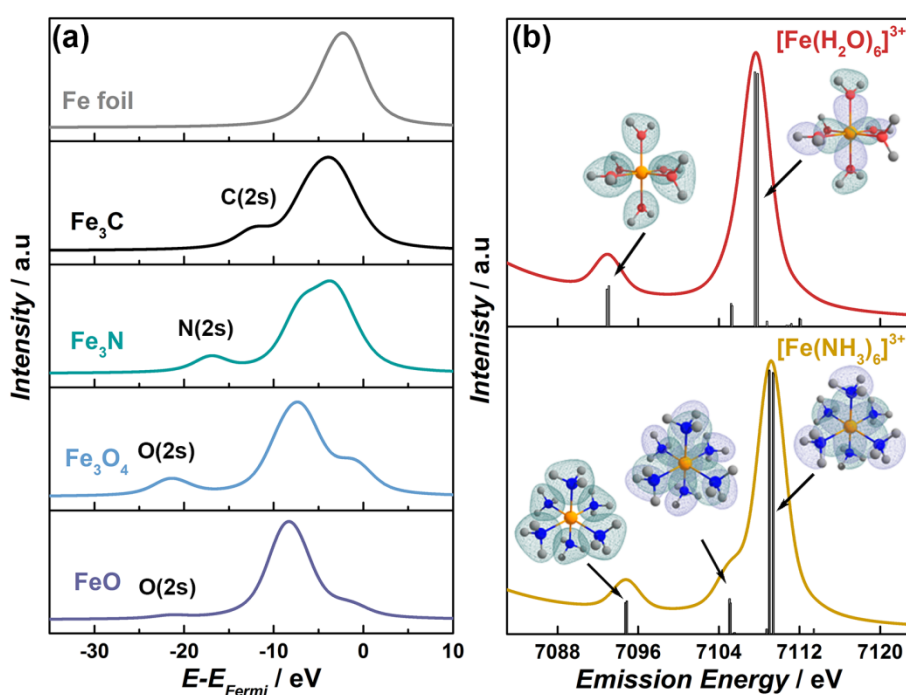
Fig. 6: Calculated VTC-$K\beta$ spectra for a a-Fe, Fe_3C, Fe_3N, Fe_3O_4, FeO, $[Fe(H_2O)_6]^{3+}$ and $[Fe(NH_3)_6]^{3+}$ compounds. Left panel (a): spectra for periodic structures calculated with the FDMNES code with the energy scale referenced against the Fermi level. The ligands states sensitivity of $K\beta$'' is outlined by the ligand orbitals label. Right panel (b): spectra for cluster models calculated with ORCA. A constant shift of +182.5 eV have been applied. Representative alpha molecular orbitals for each peaks are superimposed.

The corresponding theoretical calculations performed with the FDMNES code are provided in Fig. 6a with the extra addition of the Fe_3N theoretical spectrum that could not be measured experimentally (see the details in the supplementary information). The experimental data are well described by the theory that properly predicts the position of the $K\beta$'' line in respect to the $K\beta_{2,5}$ line position. By selecting the projected density of states on the ligands that overlaps with the metal p one (not shown), the origin of the $K\beta$'' peak was attributed to transitions from mixed ligands (*2s*) and Fe(*np*) states to Fe(*1s*) orbital, as expected. The

energy position of *2s* (and *2p*) orbitals from O, N, C ligands are properly ranked by ionization energy with nitrogen appropriately sitting in-between oxygen and carbon.[42] The theoretical VTC-$K\beta$ spectra of $[Fe(H_2O)_6]^{3+}$ and $[Fe(NH_3)_6]^{3+}$ are also presented on Fig. 6b with the visualization of representative alpha molecular orbitals from which the peaks originate. Those cluster calculations were performed with the ORCA program package following the recent and extensive work of DeBeer, Bauer, Glatzel and coworkers.[46-51] The theoretical spectra for both cations clearly show the presence of both $K\beta_{2,5}$ and $K\beta$'' lines with a significant intensity. Thus, a simple FeL_6 octahedral model with metal-ligand distance of 1.96 Å (calculated from EXAFS data) cannot reproduce the experimental spectrum of mesoNC-Fe, although the experimental XANES spectrum of $[Fe(H_2O)_6]^{3+}$ was very similar. Apart from the metal foil which does not show any $K\beta$'' peak, there are no references spectra which are anywhere close to the mesoNC-Fe spectrum.

At this point, further investigations require the understanding of the parameters that determine intensity of transitions in the VTC-$K\beta$ spectrum. With the simplest FeL_6 model, the most intense transitions derived from H_2O/NH_3 molecular orbitals belonging to the t_{1u} irreducible representation can be extracted (Fig. 6b). In octahedral symmetry, the metal *np* orbitals also transform as t_{1u} and enable the overlap with any ligand-based orbitals with the same symmetry. This is crucial for the prediction of intensities because the latter metal *p*-contribution in the molecular orbital enables the electric dipole allowed character of the transitions ($\Delta l = \pm 1$).[52] In general, only ligand orbitals interacting *via* σ-bonding will overlap significantly with the metal *p* orbitals. A possible explanation of the low $K\beta$'' intensity may involve a conjugated system around the iron center. In that case, VTC-$K\beta$ is expected to highlight mostly the σ-framework. With such coordination, the ligands atomic orbitals contribute significantly through sp^2 hybridization to the π-system decreasing inevitably their participation in the σ-framework. From this idea, we have investigated several conjugated models that we thought to potentially match the experimental XANES together with the VTC-$K\beta$ spectra. At the same time, how the intensity of $K\beta$'' can be impacted by a Fe distorted environment in small iron (III) oxyhydroxide clusters as stated by Genovese *et al.* was not investigated in this study,[53] since this structure was reported to produce formic and acetic acid in the liquid phase and none of those products were detected over the whole applied cell potential range from our mesoNC-Fe catalyst.

All geometry optimizations are detailed in the supplementary information while the optimized models can be visualized in Fig. 7. The first type of model considers periodic slabs

based on the nitrogen doped graphene structure with four pyridinic nitrogen coordinating the iron cation (Slab-FeN$_4$). The top coordination of iron was completed either by a water molecule (Slab-FeN$_4$-H$_2$O) or by a hydroxyl group (Slab-FeN$_4$-OH). The second type of model is based on the FePc complex, with a coordination completed by one hydroxyl (FePc-OH), one water molecule (FePc-H$_2$O), one hydroxyl plus one water molecule (FePc-OH-H$_2$O), and two water molecules (FePc-2H$_2$O). Those structures were inspired by the work of Zitolo, *et al.* who have shown that a porphyrinic geometry could match with the best accuracy the XANES data.[19]
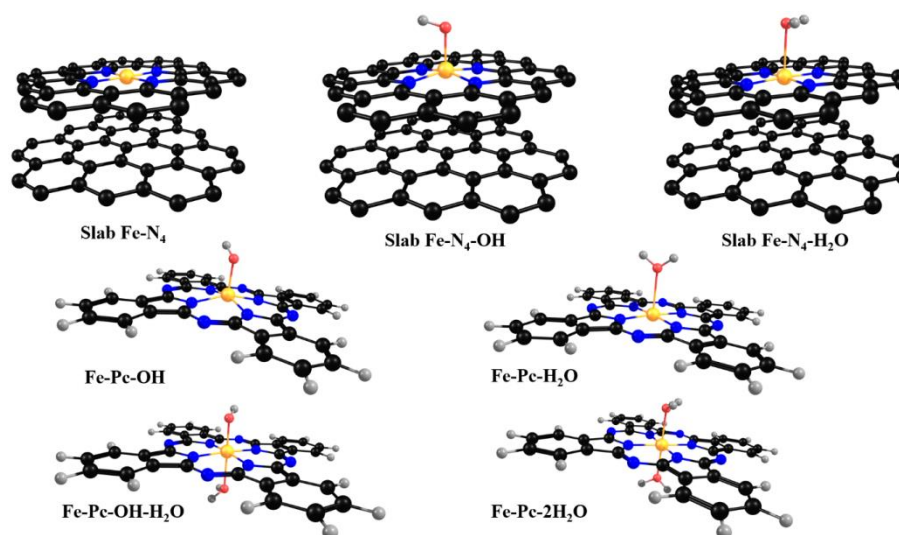
Fig. 7: DFT-optimized geometry for potential local environments of the iron active site in their most stable multiplicity state.

The accuracy of the FDMNES code related to the simulation of Fe *K*-edge absorption spectra was evaluated with reference compounds (Fig. S8): a reasonable agreement between theory and experiment is obtained with our calculation parameters. The main discrepancies are observed in the pre-edge region especially for Mott insulators such as FeO, α-Fe$_2$O$_3$, and Fe$_3$O$_4$ for which the energy separation between Fe(*3d*) and Fe(*4p*) metal orbitals is poorly predicted.[54] Then, the XANES spectra of previously optimized models are compared against the HERFD-XANES spectrum of mesoNC-Fe measured at the iron $K\beta_{1,3}$ energy (Fig. S9). The theoretical calculations are used here as a tool to exclude the models producing spectra obviously too far from the experimental results. Ultimately, the Fe-Pc-OH, Fe-Pc-2H$_2$O and FePc-OH-H$_2$O structures provide the greatest agreement as shown in Fig. 8a. The concurrence with the Fe-Pc-OH spectrum is lesser in the main-edge region which suggests that the octahedral symmetry is better suited than a square pyramidal symmetry. Furthermore, the peak in the pre-edge region of the Fe-Pc-2H$_2$O spectrum has a much lower intensity compared to the experimental data. This is because the octahedral symmetry of Fe-Pc-2H$_2$O

presents only a small axial distortion restricting the *3d-4p* mixing (*d*(Fe-N) = 1.96 Å *vs.* *d*(Fe-O) = 2.09 Å). According to XANES spectroscopy, FePc-OH-H$_2$O would be the best structural model.
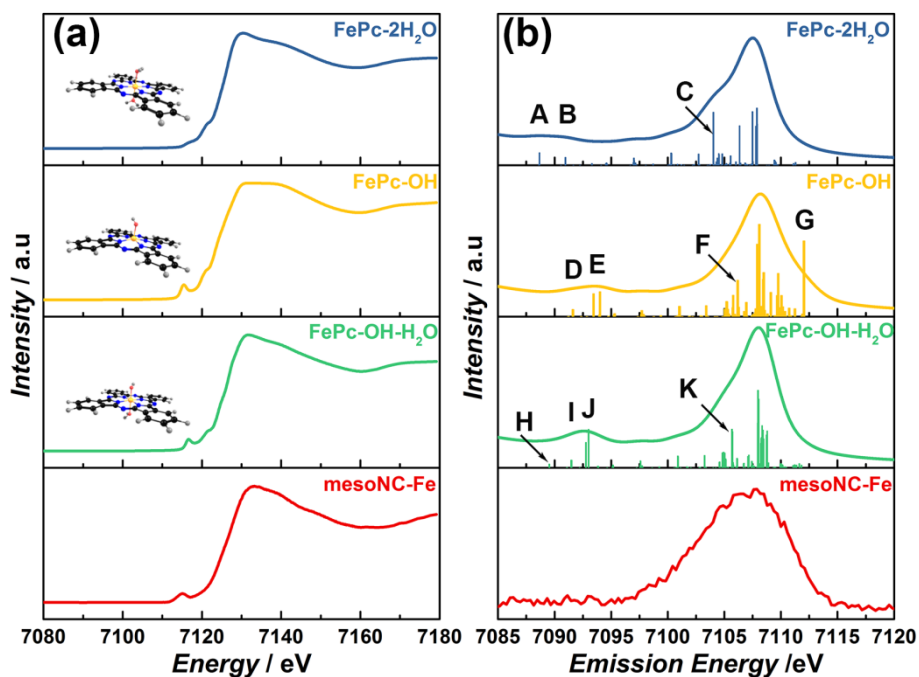
Fig. 8: Comparison of experiments and theory for HERFD-XANES and VTC-*Kβ* spectroscopies using FePc-2H$_2$O, FePc-OH, FePc-HO-HO. Left panel (a): XANES spectrum of mesoNC-Fe (2) compared against FDMNES calculations, Right panel (b): VTC-*Kβ* spectrum of mesoNC-Fe (2) compared against ORCA calculations. A constant shift of +182.5 eV have been applied.

The VTC-XES experimental spectrum and the ORCA calculations are further considered, as shown in Fig. 8b. A general observation is that the three structural models lead to VTC-*Kβ* spectra with a broad *Kβ*$_{2,5}$ line and a weak intensity for the crossover peak (*Kβ*''), or almost non-existent for the Fe-Pc-2H$_2$O model. The calculated spectra are now in much better agreement with the experimental data, especially for the *Kβ*$_{2,5}$ region. However, the intensity of the *Kβ*'' and the width of the *Kβ*$_{2,5}$ lines are respectively stronger and sharper than the experiments. This could be due to a difference of energy resolution between calculations and experiment. Besides, the current level of theory does not allow to include the effect of multiplet interactions which may further broaden the predicted *Kβ*$_{2,5}$ and *Kβ*'' lines.

14

Group Orbital	O_{H2O} *2s*	N_4 *2s*	O_{OH} *2s*
FePc-2H₂O	**A**	**B**	--
FePc-OH	--	**D**	**E**
FePc-OH-H₂O	**H**	**I**	**J**

Kβ₂,₅ assignment

Group Orbital	O_{H2O} and O_{OH} *2p*	Phtalocyanine *2p*	O_{OH} *2p*
FePc-2H₂O	**C**		
FePc-OH	**F**		**G**
FePc-OH-H₂O	**K**		
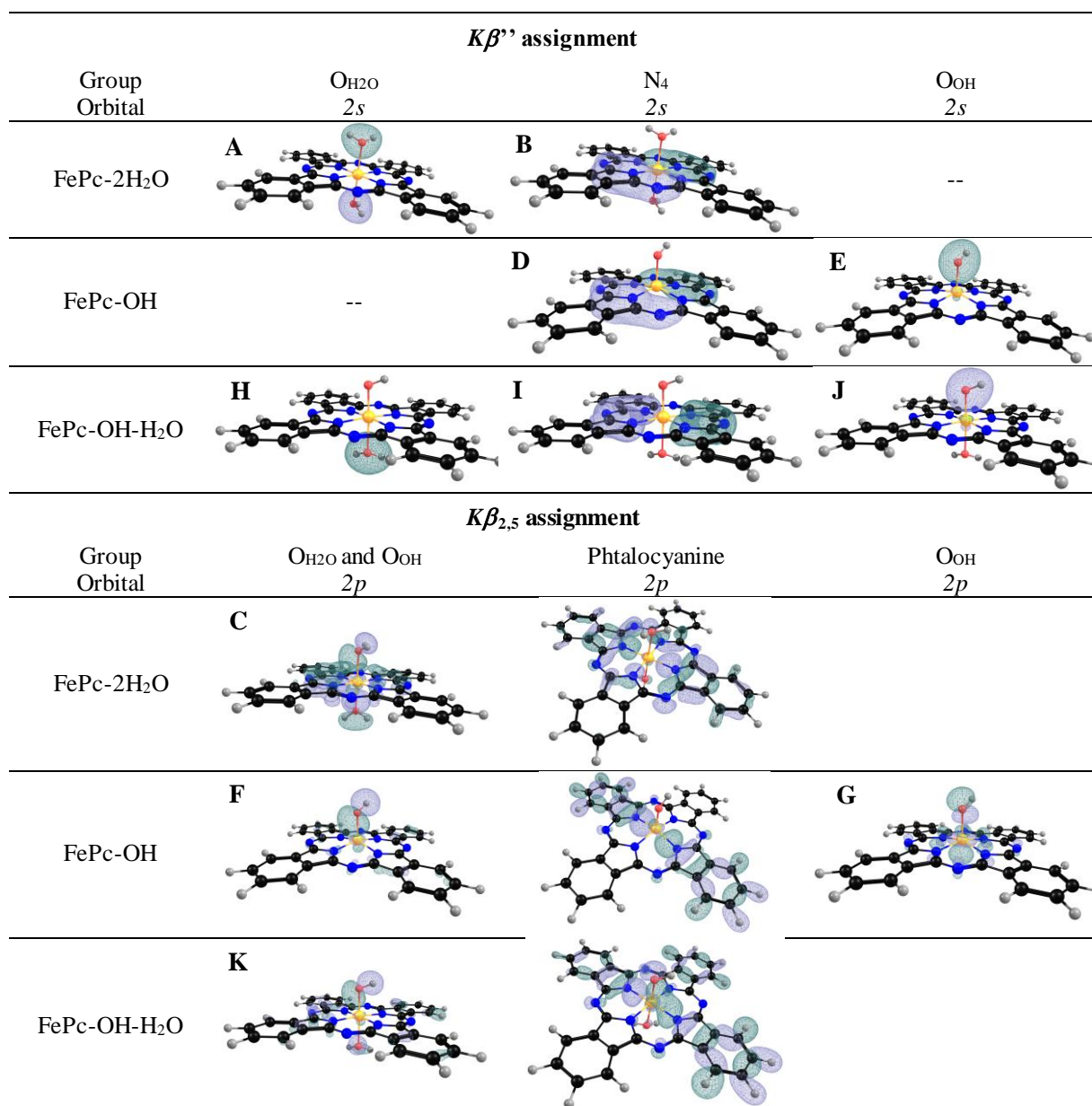
Fig. 9: Representative donor orbitals corresponding to each of the assign regions of the *Kβ''* and *Kβ₂,₅* peaks.

Fig. 9 presents the assignment of the transitions labeled by letter in the calculated valence-to-core spectra. The *Kβ₂,₅* line arises from electronic transitions from ligands *2p* into Fe *1s* orbitals. The most intense peaks are due to transitions from a mixed of Fe-O/N/C *2p* based molecular orbitals from the phtalocyanine σ-framework. All three models present a shoulder on the lower energy side which is mainly related to O_{H2O} and O_{OH} *2p* orbitals (C, F, K). The FePc-OH has an additional shoulder on the higher energy side due to a different contribution of O_{OH} *2p* orbitals (G). The *Kβ''* feature arises from electronic transitions from O *2s* and N *2s* into Fe *1s* orbitals. The N *2s* contributions appear at similar energies in all spectra (labeled as B, D, I in Fig. 8 and 10). For FePc-2H₂O, the transitions from O_{H2O} *2s* (A) orbital are at a lower energy than N_4 *2s* (B) orbital. Inversely with the FePc-OH model, O_{OH} *2s* (E) is located

15

at a higher energy than N$_4$ *2s* (D). The intermediate model FePc-OH-H$_2$O has all three transitions appearing consistently in the order O$_{H2O}$ *2s* (H), N$_4$ *2s* (I), and O$_{OH}$ *2s* (J) from lower to higher energy. Considering the intensities, only the transitions related to hydroxyl groups lead to the appearance of a significant peak. The $K\beta$'' component of the water ligand, has lower intensities due to the lower overlap of the donor with the acceptor orbitals, which is actually related to the distance between donor and acceptor site (d(Fe-O$_{OH}$) = 1.8-1.9 Å *vs.* d(Fe-O$_{H2O}$) = 2.1-2.2 Å). The same argument explains the higher $K\beta$'' intensity for FePc-OH-H$_2$O compared to FePc-OH due to the shorter Fe-O$_{OH}$ distance ($\approx$ 0.1 Å). Regarding the transitions involving nitrogen *2s* orbitals, the weak intensity is rather understood by the delocalization of the donor orbital on the phtalocyanine ligand as shown in Fig. 9 (B, D, I).

Thus, a porphyrinic environment completed by the coordination of water and/or hydroxyl group best describes the local environment of these atomically dispersed iron sites. Given the method of preparation, the chemical environment of iron must probably have some variations in terms of number of water/hydroxyl coordinated and iron-oxygen bond length. For this reason, it did not seem pertinent to choose a structural model among FePc-OH, FePc-2H$_2$O, and FePc-OH-H$_2$O, but many alternative models could be at least excluded during this study.

3.3. Electrochemical reduction of CO$_2$ over the mesoNC-Fe catalyst

After exploring the chemical environment of iron in mesoNC-Fe by using both experimental spectra and DFT calculations, we further investigate the catalytic performance of mesoNC-Fe in CO$_2$ electrochemical reduction reaction in this section. The performance of mesoNC-Fe in the electrocatalytic reduction of carbon dioxide was first evaluated by linear sweep voltammetry (LSV) (Fig. S10a). The current density in the N$_2$-saturated KHCO$_3$ solution ($j(N_2)$) is attributed to hydrogen evolution reaction (HER). Apparently, after introducing CO$_2$ in the KHCO$_3$ (0.1 M) solution, the current density of $j(CO_2)$ for mesoNC-Fe becomes higher than that of $j(N_2)$. We first investigate the pH effect on the current density when the LSV is performed (Fig. S11). The value of $j(N_2)$ increases as the pH value of the solution decreases, but is still much lower than the value in the CO$_2$ saturated KHCO$_3$ solution. This indicates that in the CO$_2$-saturated solutions both the electrochemical reduction of CO$_2$ and HER contribute to $j(CO_2)$.

In order to elucidate the role of the nitrogen-doped carbon structure in mesoNC-Fe in CO$_2$ electroreduction reaction, two reference samples (microNC and mesoNC) were first tested (see Experimental Section for the details). No liquid-phase product was

detected after each experiment over the whole applied cell potential range, and CO and H_2 are the only detectable reduction products. The FE_{CO} of microNC displays a volcano-like curve over the whole applied cell potential range with the maximum FE_{CO} of ~33% at V_{RHE} of -0.93 V (Fig. 10a). Surprisingly, the mesoNC sample with a higher surface area further promotes CO production with the maximum FE_{CO} of ~72% at V_{RHE} of -0.93 V (Fig. 10a). **The electroreduction activity of CO_2 to CO for nitrogen-doped carbon materials has been attributed to the presence of pyridinic- and quaternary-N species, which facilitate the transfer of a proton-electron pair to CO_2.[55] Moreover, the single Zn sites in the nitrogen-doped carbon matrix ($Zn-N_x$) was also proved to promote the CO_2 electroreduction performance by facilitating the formation of *COOH.[56, 57] Hence, it cannot be discarded that the remaining Zn also contributes in the electroreduction of CO_2 to CO.**
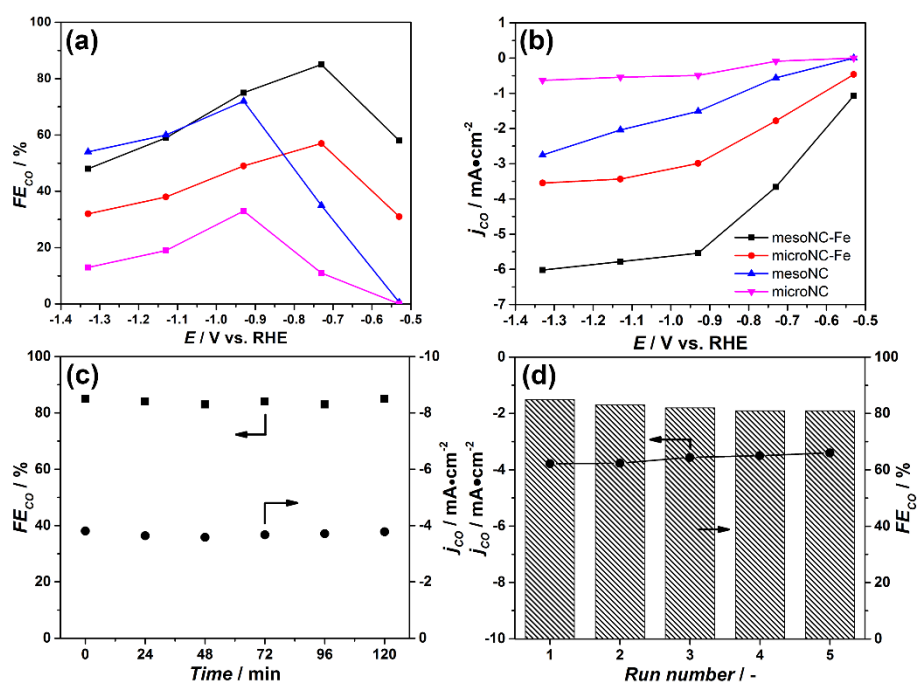
Fig. 10: FE_{CO} (a) and j_{CO} (b) of mesoNC-Fe (black) microNC-Fe (red) mesoNC (blue) and microNC (pink) in CO_2 reduction to CO; stability (c) and reusability (d) test of mesoNC-Fe in electrocatalytic reduction of CO_2 at -0.73 V vs RHE. Each recycling test lasts 120 min.

Then, the catalytic performance of mesoNC-Fe in CO_2 electroreduction reaction was further studied. As shown in Fig. 10a, after incorporating these atomically dispersed iron sites in the mesoNC matrix, the maximum FE_{CO} and the corresponding j_{CO} further increase to 85% and -3.7 mA cm^{-2}, respectively. As mesoNC and mesoNC-Fe show a similar electrochemically active surface area (ECSA) (Fig. S12d), we demonstrate that these atomically dispersed iron sites in mesoNC-Fe exhibit a higher activity than nitrogen dopants.

At the same time, the over-potential at the maximum FE_{CO} of mesoNC-Fe also shifts to V_{RHE} of -0.73 V (Fig. 10a). Previous studies have shown that CO_2 electroreduction to CO in general proceeds through the adsorbed intermediates: *COOH and *CO, where * represents the active site.[58] Hence, the free energy changes (ΔG) during the formation of *COOH and *CO on mesoNC-Fe and mesoNC catalysts are compared by using theoretical calculations with the model built in Section 3.2 (Fig. S13). **Obviously, the atomically dispersed Fe center with hydroxyl ligand (*i*) decreases the free energy barriers of *COOH formation (Fig. S13a); and (*ii*) destabilizes the adsorption of *H, which to some extent enhances the adsorption of *COOH and *CO (Fig. S13b), thereby promoting CO_2 electroreduction to CO at lower overpotentials. Moreover, a slope of ~123 mV dec^{-1} was observed at the low-overpotential region of Tafel curve, indicating that the initial electron transfer to CO_2 to form *COOH intermediates is the rate-determining step (Fig. S14). We should also acknowledge that the electron transfer, decoupled from proton transfer, can also be operative in this regime.**

Finally, in order to highlight the advantages of the SiO_2-protective strategy in this study, a microNC-Fe sample prepared by direct pyrolysis of ZIF-8-Fe was also tested. As shown in Fig. 10a and b, microNC-Fe exhibits a lower FE_{CO} and j_{CO} than that of mesoNC-Fe over the whole potential range, with the maximum FE_{CO} of ~57% and the corresponding j_{CO} of -1.9 mA cm^{-2} at V_{RHE} of -0.73 V. Interestingly, mesoNC-Fe and microNC-Fe show a good relationship between the double layer capacitance (C_{dl}) (5.88 mF cm^{-2} *versus* 3.05 mF cm^{-2}) and j_{CO} (3.7 mA cm^{-2} *versus* 1.9 mA cm^{-2}), indicating that the accessible active sites exhibit a similar activity in these two samples (Fig. S12d). Thus, compared to microNC-Fe, **the higher performance of mesoNC-Fe can be explained from the following aspects: (*i*) the larger surface area enables more atomically dispersed active sites accessible for CO_2 electroreduction; and (*ii*) the absence of iron nanoparticles to a large extent inhibits the HER reaction, in which H_2 is mainly produced. Hence, the synergetic effect of the atomically dispersed active sites in the carbon matrix makes mesoNC-Fe a more efficient catalyst for CO production compared to microNC-Fe.** The maximum FE_{CO} and the corresponding j_{CO} of mesoNC-Fe is comparable to those of nitrogen-doped carbon supported iron catalysts reported recently from other groups (Table S5). Finally, the stability and reusability of the mesoNC-Fe catalyst was also investigated, as presented in Fig. 10c and d. At the optimal V_{RHE} of -0.73 V, the mesoNC-Fe catalyst exhibits a stable j_{CO} and FE_{CO} during CO_2 electroreduction reaction and can be used at least four times without obvious

deactivation, implying the high stability of Fe-N coordination environment in the carbon matrix (Fig. S16).

4. CONCLUSIONS

In this work, a SiO_2-protective approach was reported to synthesize mesoporous NC with atomically dispersed iron sites (mesoNC-Fe) from a Fe-containing ZIF-8 template. This approach consists of hydrolysis of TMOS in ZIF-8-Fe, high-temperature pyrolysis and SiO_2 removal. We demonstrate that the presence of SiO_2 during pyrolysis is crucial to retain a high surface area in the mesoporous carbon matrix, and to hinders the formation of iron (oxide) nanoparticles. A series of X-ray spectroscopies, including HERFD-XANES, EXAFS and valence-to-core X-ray emission spectroscopies together with theoretical calculations allow us to elucidate the chemical environment of the non-crystalline iron species in mesoNC-Fe: a porphyrinic environment around iron, which is completed by H_2O/OH moieties. The mesoNC-Fe catalyst exhibits much higher FE_{CO} and j_{CO} compared to its counterparts mesoNC and microNC-Fe. This can be explained from two aspects: (i) the iron center coordinating in the porphyrinic environment with OH/H_2O moieties in mesoNC-Fe decreases the free energy barriers of *COOH formation and destabilizes the adsorption of *H; (ii) more active sites can be accessible during catalysis because of the higher surface area in the carbon structure of mesoNC-Fe than that of microNC-Fe. Our results demonstrate that HERFD-XANES and VTC-$K\beta$ spectroscopies combined with theory are a powerful tool to explore the coordination environment in these and similar atomically dispersed catalysts.

REFERENCES

[1] C. Costentin, S. Drouet, M. Robert, J.-M. Savéant, A Local Proton Source Enhances CO_2 Electroreduction to CO by a Molecular Fe Catalyst, Science, 338 (2012) 90-94.

[2] R. Banerjee, A. Phan, B. Wang, C. Knobler, H. Furukawa, M. O'Keeffe, O.M. Yaghi, High-Throughput Synthesis of Zeolitic Imidazolate Frameworks and Application to CO_2 Capture, Science, 319 (2008) 939-943.

[3] T. Schaub, R.A. Paciello, A Process for the Synthesis of Formic Acid by CO2 Hydrogenation: Thermodynamic Aspects and the Role of CO, Angewandte Chemie International Edition, 50 (2011) 7278-7282.

[4] S. Kattel, P.J. Ramírez, J.G. Chen, J.A. Rodriguez, P. Liu, Active sites for CO_2 hydrogenation to methanol on Cu/ZnO catalysts, Science, 355 (2017) 1296-1299.

[5] N. Ulagappan, H. Frei, Mechanistic Study of CO2 Photoreduction in Ti Silicalite Molecular Sieve by FT-IR Spectroscopy, The Journal of Physical Chemistry A, 104 (2000) 7834-7839.

[6] R. Wang, X. Sun, S. Ould-Chikh, D. Osadchii, F. Bai, F. Kapteijn, J. Gascon, Metal-Organic-Framework-Mediated Nitrogen-Doped Carbon for CO2 Electrochemical Reduction, ACS Applied Materials & Interfaces, (2018).

[7] W. Zhu, R. Michalsky, Ö. Metin, H. Lv, S. Guo, C.J. Wright, X. Sun, A.A. Peterson, S. Sun, Monodisperse Au Nanoparticles for Selective Electrocatalytic Reduction of CO2 to CO, Journal of the American Chemical Society, 135 (2013) 16833-16836.

[8] M. Ma, B.J. Trześniewski, J. Xie, W.A. Smith, Selective and Efficient Reduction of Carbon Dioxide to Carbon Monoxide on Oxide-Derived Nanostructured Silver Electrocatalysts, Angewandte Chemie International Edition, 55 (2016) 9748-9752.

[9] M. Ma, K. Djanashvili, W.A. Smith, Controllable Hydrocarbon Formation from the Electrochemical Reduction of CO2 over Cu Nanowire Arrays, Angewandte Chemie, 128 (2016) 6792-6796.

[10] W.F. Chen, K. Sasaki, C. Ma, A.I. Frenkel, N. Marinkovic, J.T. Muckerman, Y. Zhu, R.R. Adzic, Hydrogen‐Evolution Catalysts Based on Non‐Noble Metal Nickel–Molybdenum Nitride Nanosheets, Angewandte Chemie International Edition, 51 (2012) 6131-6135.

[11] S. Back, M.S. Yeom, Y. Jung, Active Sites of Au and Ag Nanoparticle Catalysts for CO2 Electroreduction to CO, ACS Catalysis, 5 (2015) 5089-5096.

[12] X. Sun, A.I.O. Suarez, M. Meijerink, T. van Deelen, S. Ould-Chikh, J. Zečević, K.P. de Jong, F. Kapteijn, J. Gascon, Manufacture of highly loaded silica-supported cobalt Fischer–Tropsch catalysts from a metal organic framework, Nature Communications, 8 (2017) 1680.

[13] X. Sun, S. Sartipi, F. Kapteijn, J. Gascon, Effect of pretreatment atmosphere on the activity and selectivity of Co/mesoHZSM-5 for Fischer-Tropsch synthesis, New Journal of Chemistry, 40 (2016) 4167-4177.

[14] F. Pan, H. Zhang, K. Liu, D. Cullen, K. More, M. Wang, Z. Feng, G. Wang, G. Wu, Y. Li, Unveiling Active Sites of CO2 Reduction on Nitrogen-Coordinated and Atomically Dispersed Iron and Cobalt Catalysts, ACS Catalysis, 8 (2018) 3116-3122.

[15] T. Rodenas, S. Beeg, I. Spanos, S. Neugebauer, F. Girgsdies, G. Algara-Siller, P.P.M. Schleker, P. Jakes, N. Pfänder, M. Willinger, M. Greiner, G. Prieto, R. Schlögl, S. Heumann, 2D Metal Organic Framework-Graphitic Carbon Nanocomposites as Precursors for High-Performance O2-Evolution Electrocatalysts, Advanced Energy Materials, 8 (2018) 1802404.

[16] T.N. Huan, N. Ranjbar, G. Rousse, M. Sougrati, A. Zitolo, V. Mougel, F. Jaouen, M. Fontecave, Electrochemical Reduction of CO2 Catalyzed by Fe-N-C Materials: A Structure–Selectivity Study, ACS Catalysis, 7 (2017) 1520-1525.

[17] W. Liu, L. Zhang, X. Liu, X. Liu, X. Yang, S. Miao, W. Wang, A. Wang, T. Zhang, Discriminating Catalytically Active FeNx Species of Atomically Dispersed Fe–N–C Catalyst for Selective Oxidation of the C–H Bond, Journal of the American Chemical Society, 139 (2017) 10790-10798.

[18] H. Fei, J. Dong, Y. Feng, C.S. Allen, C. Wan, B. Volosskiy, M. Li, Z. Zhao, Y. Wang, H. Sun, P. An, W. Chen, Z. Guo, C. Lee, D. Chen, I. Shakir, M. Liu, T. Hu, Y. Li, A.I. Kirkland, X. Duan, Y. Huang, General synthesis and definitive structural identification of MN4C4 single-atom catalysts with tunable electrocatalytic activities, Nature Catalysis, 1 (2018) 63-72.

[19] A. Zitolo, V. Goellner, V. Armel, M.-T. Sougrati, T. Mineva, L. Stievano, E. Fonda, F. Jaouen, Identification of catalytic sites for oxygen reduction in iron- and nitrogen-doped graphene materials, Nature Materials, 14 (2015) 937.

[20] X. Sun, A.I. Olivos-Suarez, L. Oar-Arteta, E. Rozhko, D. Osadchii, A. Bavykina, F. Kapteijn, J. Gascon, Metal–Organic Framework Mediated Cobalt/Nitrogen-Doped Carbon Hybrids as Efficient and Chemoselective Catalysts for the Hydrogenation of Nitroarenes, ChemCatChem, 9 (2017) 1854-1862.

[21] X. Sun, A.I. Olivos-Suarez, D. Osadchii, M.J.V. Romero, F. Kapteijn, J. Gascon, Single cobalt sites in mesoporous N-doped carbon matrix for selective catalytic hydrogenation of nitroarenes, Journal of Catalysis, 357 (2018) 20-28.

[22] Y. Deng, Y. Dong, G. Wang, K. Sun, X. Shi, L. Zheng, X. Li, S. Liao, Well-Defined ZIF-Derived Fe–N Codoped Carbon Nanoframes as Efficient Oxygen Reduction Catalysts, ACS Applied Materials & Interfaces, 9 (2017) 9699-9709.

[23] Y.-Z. Chen, C. Wang, Z.-Y. Wu, Y. Xiong, Q. Xu, S.-H. Yu, H.-L. Jiang, From Bimetallic Metal-Organic Framework to Porous Carbon: High Surface Area and Multicomponent Active Dopants for Excellent Electrocatalysis, Advanced Materials, 27 (2015) 5010-5016.

[24] P. Yin, T. Yao, Y. Wu, L. Zheng, Y. Lin, W. Liu, H. Ju, J. Zhu, X. Hong, Z. Deng, G. Zhou, S. Wei, Y. Li, Single Cobalt Atoms with Precise N-Coordination as Superior Oxygen Reduction Reaction Catalysts, Angewandte Chemie International Edition, 55 (2016) 10800-10805.

[25] L. Zhang, Z. Su, F. Jiang, L. Yang, J. Qian, Y. Zhou, W. Li, M. Hong, Highly graphitized nitrogen-doped porous carbon nanopolyhedra derived from ZIF-8 nanocrystals as efficient electrocatalysts for oxygen reduction reactions, Nanoscale, 6 (2014) 6590-6602.

[26] N.L. Torad, M. Hu, Y. Kamachi, K. Takai, M. Imura, M. Naito, Y. Yamauchi, Facile synthesis of nanoporous carbons with controlled particle sizes by direct carbonization of monodispersed ZIF-8 crystals, Chemical Communications, 49 (2013) 2521-2523.

[27] F. Sastre, M.J. Muñoz-Batista, A. Kubacka, M. Fernández-García, W.A. Smith, F. Kapteijn, M. Makkee, J. Gascon, Efficient Electrochemical Production of Syngas from CO2 and H2O by using a Nanostructured Ag/g-C3N4 Catalyst, ChemElectroChem, 3 (2016) 1497-1502.

[28] H. Fei, J. Dong, M.J. Arellano-Jiménez, G. Ye, N. Dong Kim, E.L.G. Samuel, Z. Peng, Z. Zhu, F. Qin, J. Bao, M.J. Yacaman, P.M. Ajayan, D. Chen, J.M. Tour, Atomic cobalt on nitrogen-doped graphene for hydrogen generation, Nature Communications, 6 (2015) 8668.

[29] J. Tang, R.R. Salunkhe, J. Liu, N.L. Torad, M. Imura, S. Furukawa, Y. Yamauchi, Thermal Conversion of Core–Shell Metal–Organic Frameworks: A New Method for Selectively Functionalized Nanoporous Hybrid Carbon, Journal of the American Chemical Society, 137 (2015) 1572-1580.

[30] S. Wang, L. Shang, L. Li, Y. Yu, C. Chi, K. Wang, J. Zhang, R. Shi, H. Shen, G.I.N. Waterhouse, S. Liu, J. Tian, T. Zhang, H. Liu, Metal–Organic-Framework-Derived Mesoporous Carbon Nanospheres Containing Porphyrin-Like Metal Centers for Conformal Phototherapy, Advanced Materials, 28 (2016) 8379-8387.

[31] J. Casanovas, J.M. Ricart, J. Rubio, F. Illas, J.M. Jiménez-Mateos, Origin of the Large N 1s Binding Energy in X-ray Photoelectron Spectra of Calcined Carbonaceous Materials, Journal of the American Chemical Society, 118 (1996) 8071-8076.

[32] J. GARCIA, A. BIANCONI, M. BENFATTO, C. NATOLI, R., COORDINATION GEOMETRY OF TRANSITION METAL IONS IN DILUTE SOLUTIONS BY XANES, J. Phys. Colloques, 47 (1986) C8-49-C48-54.

[33] W. Ju, A. Bagger, G.-P. Hao, A.S. Varela, I. Sinev, V. Bon, B. Roldan Cuenya, S. Kaskel, J. Rossmeisl, P. Strasser, Understanding activity and selectivity of metal-nitrogen-doped carbon catalysts for electrochemical reduction of CO2, Nature Communications, 8 (2017) 944.

[34] N. Kosugi, T. Yokoyama, K. Asakura, H. Kuroda, Polarized Cu K-edge XANES of square planar CuCl42− ion. Experimental and theoretical evidence for shake-down phenomena, Chemical Physics, 91 (1984) 249-256.

[35] M. Wilke, F.o. Farges, G.E. Brown, Jr., P.-E. Petit, F.o. Martin, Oxidation state and coordination of Fe in minerals: An Fe K-XANES spectroscopic study, American Mineralogist, 86 (2001) 714-730.

[36] T.E. Westre, P. Kennepohl, J.G. DeWitt, B. Hedman, K.O. Hodgson, E.I. Solomon, A Multiplet Analysis of Fe K-Edge 1s → 3d Pre-Edge Features of Iron Complexes, Journal of the American Chemical Society, 119 (1997) 6297-6314.

[37] J.J. Rehr, R.C. Albers, Theoretical approaches to x-ray absorption fine structure, Reviews of Modern Physics, 72 (2000) 621-654.

[38] W. Liang, J. Chen, Y. Liu, S. Chen, Density-Functional-Theory Calculation Analysis of Active Sites for Four-Electron Reduction of O2 on Fe/N-Doped Graphene, ACS Catalysis, 4 (2014) 4170-4177.

[39] N. Leonard, W. Ju, I. Sinev, J. Steinberg, F. Luo, A.S. Varela, B. Roldan Cuenya, P. Strasser, The chemical identity, state and structure of catalytically active centers during the electrochemical CO2 reduction on porous Fe–nitrogen–carbon (Fe–N–C) materials, Chemical Science, 9 (2018) 5064-5073.

[40] Y. Mun, M.J. Kim, S.-A. Park, E. Lee, Y. Ye, S. Lee, Y.-T. Kim, S. Kim, O.-H. Kim, Y.-H. Cho, Y.-E. Sung, J. Lee, Soft-template synthesis of mesoporous non-precious metal catalyst with Fe-Nx/C active sites for oxygen reduction reaction in fuel cells, Applied Catalysis B: Environmental, 222 (2018) 191-199.

[41] P. Glatzel, U. Bergmann, High resolution 1s core hole X-ray spectroscopy in 3d transition metal complexes—electronic and structural information, Coordination Chemistry Reviews, 249 (2005) 65-95.

[42] U. Bergmann, C.R. Horne, T.J. Collins, J.M. Workman, S.P. Cramer, Chemical dependence of interatomic X-ray transition energies and intensities – a study of Mn Kβ″ and Kβ2,5 spectra, Chemical Physics Letters, 302 (1999) 119-124.

[43] V.A. Safonov, L.N. Vykhodtseva, Y.M. Polukarov, O.V. Safonova, G. Smolentsev, M. Sikora, S.G. Eeckhout, P. Glatzel, Valence-to-Core X-ray Emission Spectroscopy Identification of Carbide Compounds in Nanocrystalline Cr Coatings Deposited from Cr(III) Electrolytes Containing Organic Substances, The Journal of Physical Chemistry B, 110 (2006) 23192-23196.

[44] S.G. Eeckhout, O.V. Safonova, G. Smolentsev, M. Biasioli, V.A. Safonov, L.N. Vykhodtseva, M. Sikora, P. Glatzel, Cr local environment by valence-to-core X-ray emission spectroscopy, Journal of Analytical Atomic Spectrometry, 24 (2009) 215-223.

[45] K.M. Lancaster, M. Roemelt, P. Ettenhuber, Y. Hu, M.W. Ribbe, F. Neese, U. Bergmann, S. DeBeer, X-ray Emission Spectroscopy Evidences a Central Carbon in the Nitrogenase Iron-Molybdenum Cofactor, Science, 334 (2011) 974-977.

[46] S. DeBeer George, F. Neese, Calibration of Scalar Relativistic Density Functional Theory for the Calculation of Sulfur K-Edge X-ray Absorption Spectra, Inorganic Chemistry, 49 (2010) 1849-1853.

[47] C.J. Pollock, S. DeBeer, Valence-to-Core X-ray Emission Spectroscopy: A Sensitive Probe of the Nature of a Bound Ligand, Journal of the American Chemical Society, 133 (2011) 5594-5601.

[48] C.J. Pollock, S. DeBeer, Insights into the Geometric and Electronic Structure of Transition Metal Centers from Valence-to-Core X-ray Emission Spectroscopy, Accounts of Chemical Research, 48 (2015) 2967-2975.

[49] M. Bauer, HERFD-XAS and valence-to-core-XES: new tools to push the limits in research with hard X-rays?, Physical Chemistry Chemical Physics, 16 (2014) 13827-13837.

[50] E. Gallo, P. Glatzel, Valence to Core X-ray Emission Spectroscopy, Advanced Materials, 26 (2014) 7730-7746.

[51] F. Neese, The ORCA program system, Wiley Interdisciplinary Reviews: Computational Molecular Science, 2 (2012) 73-78.

[52] N. Lee, T. Petrenko, U. Bergmann, F. Neese, S. DeBeer, Probing Valence Orbital Composition with Iron Kβ X-ray Emission Spectroscopy, Journal of the American Chemical Society, 132 (2010) 9715-9727.

[53] C. Genovese, M.E. Schuster, E.K. Gibson, D. Gianolio, V. Posligua, R. Grau-Crespo, G. Cibin, P.P. Wells, D. Garai, V. Solokha, S. Krick Calderon, J.J. Velasco-Velez, C. Ampelli, S. Perathoner, G. Held, G. Centi, R. Arrigo, Operando spectroscopy study of the carbon dioxide electro-reduction by iron species on nitrogen-doped carbon, Nature Communications, 9 (2018) 935.

[54] J. Hubbard, B.H. Flowers, Electron correlations in narrow energy bands, Proceedings of the Royal Society of London. Series A. Mathematical and Physical Sciences, 276 (1963) 238-257.

[55] P.P. Sharma, J. Wu, R.M. Yadav, M. Liu, C.J. Wright, C.S. Tiwary, B.I. Yakobson, J. Lou, P.M. Ajayan, X.-D. Zhou, Nitrogen-Doped Carbon Nanotube Arrays for High-Efficiency Electrochemical Reduction of CO2: On the Understanding of Defects, Defect Density, and Selectivity, Angewandte Chemie International Edition, 54 (2015) 13701-13705.

[56] F. Yang, P. Song, X. Liu, B. Mei, W. Xing, Z. Jiang, L. Gu, W. Xu, Highly Efficient CO2 Electroreduction on ZnN4-based Single-Atom Catalyst, Angewandte Chemie International Edition, 57 (2018) 12303-12307.

[57] Z. Chen, K. Mou, S. Yao, L. Liu, Zinc-Coordinated Nitrogen-Codoped Graphene as an Efficient Catalyst for Selective Electrochemical Reduction of CO2 to CO, ChemSusChem, 11 (2018) 2944-2952.

[58] V. Tripkovic, M. Vanin, M. Karamad, M.E. Björketun, K.W. Jacobsen, K.S. Thygesen, J. Rossmeisl, Electrochemical CO2 and CO Reduction on Metal-Functionalized Porphyrin-like Graphene, The Journal of Physical Chemistry C, 117 (2013) 9187-9195.